JACS
JOURNAL OF THE AMERICAN CHEMICAL SOCIETY
pubs.acs.org/JACS
Article

Lanthanide Doping into All-Inorganic Heterometallic Halide Layered Double Perovskite Nanocrystals for Multimodal Visible and Near-Infrared Emission

Tong Cai, Wenwu Shi, Rongzhen Wu, Chun Chu, Na Jin, Junyu Wang, Weiwei Zheng, Xinzhong Wang,* and Ou Chen*

Cite This: J. Am. Chem. Soc. 2024, 146, 3200−3209

ABSTRACT: The introduction of lanthanide ions (Ln^{3+}) into all-inorganic lead-free halide perovskites has captured significant attention in optoelectronic applications. However, doping Ln^{3+} ions into heterometallic halide layered double perovskite (LDP) nanocrystals (NCs) and their associated doping mechanisms remain unexplored. Herein, we report the first colloidal synthesis of Ln^{3+} (Yb^{3+}, Er^{3+})-doped LDP NCs utilizing a modified hot-injection method. The resulting NCs exhibit efficient near-infrared (NIR) photoluminescence in both NIR-I and NIR-II regions, achieved through energy transfer down-conversion mechanisms. Density functional theory calculations reveal that Ln^{3+} dopants preferentially occupy the Sb^{3+} cation positions, resulting in a disruption of local site symmetry of the LDP lattices. By leveraging sensitizations of intermediate energy levels, we delved into a series of Ln^{3+}-doped $Cs_4M(II)Sb_2Cl_{12}$ (M(II): Cd^{2+} or Mn^{2+}) LDP NCs via co-doping strategies. Remarkably, we observe a brightening effect of the predark states of Er^{3+} dopant in the Er^{3+}-doped $Cs_4M(II)Sb_2Cl_{12}$ LDP NCs owing to the Mn component acting as an intermediate energy bridge. This study not only advances our understanding of energy transfer mechanisms in doped NCs but also propels all-inorganic LDP NCs for a wider range of optoelectronic applications.

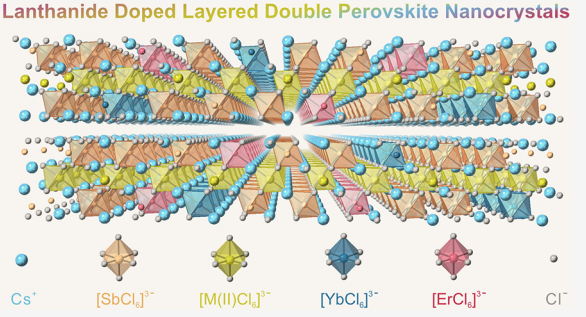

INTRODUCTION

All-inorganic lead halide perovskite ($APbX_3$, A: Cs^+, Rb^+; X: Cl^-, Br^-, I^-) nanocrystals (NCs) have garnered an unprecedented amount of attention in recent years due to their superior optoelectronic properties, holding immense potential for various applications.[1−5] Nevertheless, the toxicity of lead element inclusion and their potential impacts on environmental pollution have hindered their widespread adoption for technology commercialization.[6] To address this concern, researchers have developed an extensive library of lead-free perovskite derivatives through composition substitution and tuning and crystal dimensionality engineering.[7−9] For instance, substituting the Pb^{2+} component by either monovalent or trivalent cations of one type (e.g., M(I): Cu^+, Ag^+, or M(III): Bi^{3+}, Sb^{3+}, In^{3+}) results in low-dimensional perovskite derivatives, such as $AM(I)_2X_3$, $A_2M(I)X_3$, $A_3M(I)_2X_5$, $A_3M(III)X_6$, or $A_3M(III)_2X_9$.[10−15] Additionally, replacing every two Pb^{2+} cations with a pair of monovalent and trivalent cations leads to the formation of $A_2M(I)M(III)X_6$ (M(I): Na^+, Ag^+, K^+, In^+; M(III): Bi^{3+}, Sb^{3+}, In^{3+}, Au^{3+}, lanthanide ions, Ln^{3+}) double perovskites while retaining their three-dimensional (3D) crystal structures.[16−23] Combining both the lead-substitution and dimensionality engineering strategies, a new class of all-inorganic heterometallic halide layered double perovskites (LDPs) with a chemical formula of $A_4M(II)M(III)_2X_{12}$ (M(II): Cu^{2+}, Cd^{2+}, Mn^{2+}, Sn^{2+}, and Zn^{2+}; M(III): Bi^{3+}, Sb^{3+}, In^{3+}) has been recently discovered.[9,24−31] The LDP structure exhibits a 2D layered crystalline structure with a unique sandwiched heterometallic halide octahedra arrangement (i.e., $M(III)X_6$-$M(II)X_6$-$M(III)X_6$, Figures 1A and S1). The simultaneous incorporation of divalent and trivalent cations, and thereby the expansion of the compositional space of LDPs, provides ample opportunities for discovering new LDP materials with customizable control over their properties.[32−34]

Concurrently, doping impurity ions into perovskite NCs has proven to be an effective means for tailoring crystal structures and fine-tuning optical, magnetic, thermal, and optoelectronic properties.[35] In particular, the introduction of rare earth Ln^{3+} impurities into lead-free perovskite NCs offers several unique advantages. These include the ability to adjust multimodal photoluminescence (PL) profiles across both visible and near-

Received: October 9, 2023
Revised: January 5, 2024
Accepted: January 8, 2024
Published: January 26, 2024

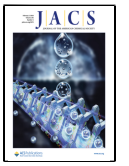

https://doi.org/10.1021/jacs.3c11164
J. Am. Chem. Soc. 2024, 146, 3200−3209

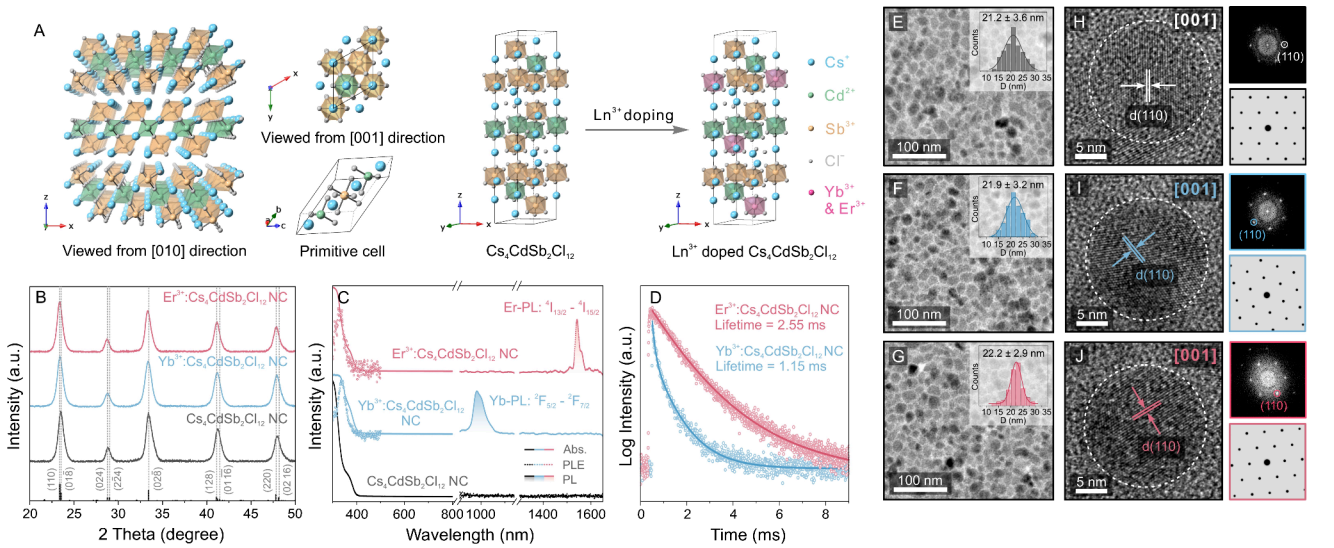

Figure 1. Characterization of undoped and Ln^{3+} (Yb^{3+} or Er^{3+})-doped $Cs_4CdSb_2Cl_{12}$ LDP NCs. (A) Schematic of undoped and Ln^{3+}-doped $Cs_4CdSb_2Cl_{12}$ LDP crystal structures. The left panel shows the 2D layered "sandwiched" structures of LDPs from the [010] viewing direction. The middle panel includes the LDP structures from the [001] viewing direction and the primitive cell of LDPs. The right panel exhibits the Ln^{3+} (Yb^{3+} or Er^{3+}) doping process in a representative LDP unit cell. (B) XRD pattern of undoped and Yb^{3+}- or Er^{3+}-doped $Cs_4CdSb_2Cl_{12}$ LDP NCs. Black bars represent the standard XRD peaks of bulk $Cs_4CdSb_2Cl_{12}$ LDPs (ICSD: 14995).[57] The Ln^{3+} (Yb^{3+} or Er^{3+}) doping concentration is 15%. (C) UV−vis absorption, PL, and PLE spectra of undoped and Yb^{3+}- or Er^{3+}-doped $Cs_4CdSb_2Cl_{12}$ LDP NCs. (D) PL lifetime decay curves of Yb^{3+}- or Er^{3+}-doped $Cs_4CdSb_2Cl_{12}$ LDP NCs monitoring the NIR PL at 983 and 1541 nm, respectively. (E−G) TEM images of (E) undoped and (F) Yb^{3+}- or (G) Er^{3+}-doped $Cs_4CdSb_2Cl_{12}$ LDP NCs. The insets are size histograms. (H−J) HR-TEM images of undoped (H), and Yb^{3+} (I) or Er^{3+} (J) doped $Cs_4CdSb_2Cl_{12}$ LDP NCs. The right panels are the corresponding fast Fourier transform (FFT) patterns (top) and computer-simulated electron diffraction patterns (bottom).

infrared (NIR) spectral ranges due to the presence of rich energy levels,[36−38] enhanced light conversion efficiency with potential quantum cutting effects,[39,40] and induction of a robust magnetic moment with both orbital and spin contributions originating from unpaired f-electrons.[41,42] Nevertheless, Ln^{3+} ions typically display a low absorption extinction coefficient due to their parity-forbidden f−f transitions.[40−42] In addition, the facile coupling between lattice vibrations and NIR transitions of neighboring Ln dopants can lead to reduced PL quantum yield (QY) through self-quenching.[43−45] To date, successful doping of Ln^{3+} into lead-free perovskite NC systems has been very limited. Reported examples include the incorporation of Ln^{3+} ions (such as Yb^{3+}, Er^{3+}, and Tb^{3+}) within $Cs_2M(I)M(III)Cl_6$ ($M(I)$: Na^+, Ag^+; $M(III)$: Bi^{3+}, In^{3+}) double perovskite NCs, resulting in enhanced optical properties in the NIR range.[46,47] Co-doping Ln^{3+} (e.g., Tb^{3+}, Er^{3+}, Sm^{3+}, Nd^{3+}) with main group trivalent metal cations (e.g., Bi^{3+}, Sb^{3+}) in $Cs_2AgInCl_6$ double perovskite NCs has also been demonstrated.[48−51] Compared to double perovskites, LDPs possess a unique 2D layered "sandwiched" crystal structure that remains largely unexplored with regard to the Ln^{3+} doping positions and energy transfer mechanisms.[9] Despite few trials of doping Ln^{3+} ions into bulk-scale LDPs,[52−54] the incorporation of Ln^{3+} dopants in nanoscale LDP materials, enabling multimodal visible/NIR emissions, has yet to be presented. Therefore, there is a significant knowledge gap in our understanding of how Ln^{3+} doping affects electronic and crystal structures and the intricate energy transfer mechanisms within Ln^{3+}-doped LDP NCs.

In this study, we report the first colloidal synthesis of Ln^{3+} (Yb^{3+}, Er^{3+}, or both)-doped heterometallic halide LDP NCs using a hot-injection approach. The introduction of Ln^{3+} dopants gave rise to distinctive NIR emission bands, which were attributed to the characteristic f−f transitions exhibited by Ln^{3+} ions within the LDP lattices. The influences of Ln^{3+} doping on the crystal lattices, optical properties, and electronic band structures were systematically investigated through a combination of experimental studies and density functional theory (DFT) calculations. Moreover, the mechanisms governing energy transfer between the NC host and Ln^{3+} dopants, as well as between different types of Ln^{3+} ion centers through intermediate energy sensitization, were examined across a series of delicately designed Ln^{3+}-doped $Cs_4CdSb_2Cl_{12}$ or $Cs_4MnSb_2Cl_{12}$ LDP NCs. Our comprehensive investigations not only provide fundamental insights into the impact of Ln^{3+} doping on the crystal and electronic structures of heterometallic halide LDP NCs but also pave the way for novel applications across diverse fields including optical data encryption, low-loss optical telecommunication, multiplexed NIR detection, and imaging.

RESULTS AND DISCUSSION

Colloidal syntheses of undoped and Ln^{3+} (Yb^{3+} or Er^{3+})-doped $Cs_4CdSb_2Cl_{12}$ LDP NCs (Figure 1A) were conducted following a modified hot-injection method (see synthetic details in the SI).[55,56] Briefly, metal precursors, including cesium acetate, cadmium acetate, antimony acetate, and either ytterbium acetate or erbium acetate, were added into a mixture of oleic acid, oleylamine, and 1-octadecene, which served as the organic capping ligand and the solvent. After complete dissolution of all metal salts, the solution was heated to 180 °C, and chlorotrimethylsilane (TMS-Cl) was rapidly injected to initiate the LDP NC nucleation. Five seconds after the injection, the reaction was quenched by cooling in an ice bath, followed by purification to remove excess ligands.

https://doi.org/10.1021/jacs.3c11164
J. Am. Chem. Soc. 2024, 146, 3200−3209

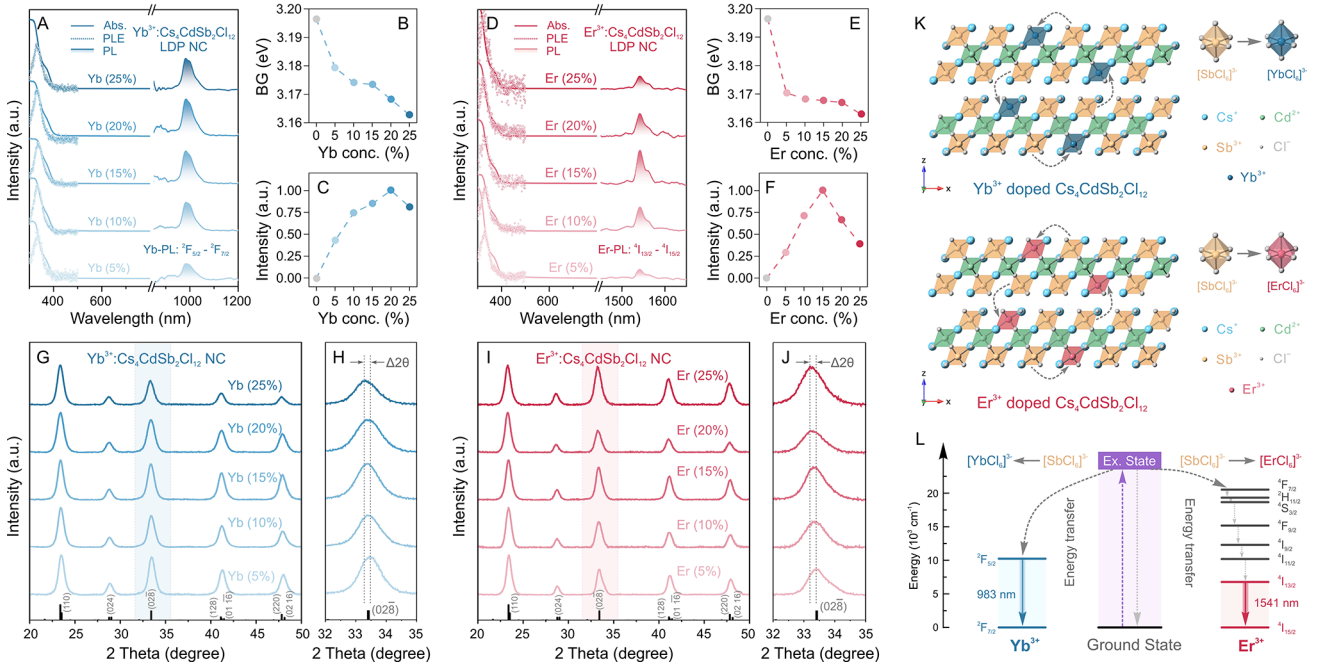

Figure 2. Effects of varied Ln^{3+} (Yb^{3+} or Er^{3+}) doping concentrations on the optical properties and crystal structures of $Cs_4CdSb_2Cl_{12}$ LDP NCs. (A) Absorption, PLE, and PL spectra of Yb^{3+}-doped $Cs_4CdSb_2Cl_{12}$ LDP NCs with different Yb^{3+} doping concentrations. (B, C) The evolution of bandgap (BG) (B) and Yb-PL intensity (C) of Yb^{3+}-doped $Cs_4CdSb_2Cl_{12}$ LDP NCs with different doping concentrations. (D) Absorption, PLE, and PL spectra of Er^{3+}-doped $Cs_4CdSb_2Cl_{12}$ LDP NCs with different Er^{3+} doping concentrations. (E, F) The evolution of bandgap (E) and Er-PL intensity (F) of Er^{3+}-doped $Cs_4CdSb_2Cl_{12}$ LDP NCs with different doping concentrations. (G) XRD patterns and (H) zoomed-in XRD patterns of Yb^{3+}-doped $Cs_4CdSb_2Cl_{12}$ LDP NCs with different Yb^{3+} doping concentrations. (I) XRD patterns and (J) zoomed-in XRD patterns of Er^{3+}-doped $Cs_4CdSb_2Cl_{12}$ LDP NCs with different Er^{3+} doping concentrations. (K) The scheme of the proposed mechanism for the energy transfer process in the Ln^{3+} (Yb^{3+} or Er^{3+})-doped $Cs_4CdSb_2Cl_{12}$ LDP crystal structures. (L) Energy level alignment for Ln^{3+} (Yb^{3+} or Er^{3+})-doped $Cs_4CdSb_2Cl_{12}$ LDPs.

X-ray diffraction (XRD) patterns confirmed that both undoped and Ln^{3+}-doped $Cs_4CdSb_2Cl_{12}$ LDP NCs exhibited a trigonal phase with a vacancy-ordered layered structure (space group: $R\bar{3}m$, Figure 1A), matching well with the standard bulk $Cs_4CdSb_2Cl_{12}$ LDPs (Figure 1B).[57] The observed peak shifts toward smaller angles in the Ln^{3+}-doped samples indicated lattice expansion due to the incorporation of Ln^{3+} dopants with larger ionic sizes (Yb^{3+}: 101 pm and Er^{3+}: 103 pm, vs Sb^{3+}: 90 pm).[58] The lattice constants for the undoped and Yb^{3+} (Er^{3+})-doped LDP NCs were determined to be a = 7.59 Å (undoped), 7.61 Å (Yb^{3+}-doped), 7.62 Å (Er^{3+}-doped) and c = 36.96 Å (undoped), 37.00 Å (Yb^{3+}-doped), 37.07 Å (Er^{3+}-doped) (Tables S1−S3). The absorption spectra of both undoped and Ln^{3+}-doped $Cs_4CdSb_2Cl_{12}$ LDP NCs exhibit a similar absorption onset around 390 nm (Figure 1C), implying minimal changes in the electronic structures and bandgap of the host LDP NCs upon doping. The bandgap values of 3.196, 3.173, and 3.167 eV were determined using Tauc plots based on the direct allowed transition mechanism for $Cs_4CdSb_2Cl_{12}$ LDP NCs and Yb^{3+}-doped and Er^{3+}-doped $Cs_4CdSb_2Cl_{12}$ LDP NCs, respectively (Figure S2). These bandgap energies are consistent with the values reported in previous experimental works as well as DFT calculations.[55,57] No PL signal was observed for the undoped $Cs_4CdSb_2Cl_{12}$ LDP NCs at room temperature (Figure 1C), likely due to fast carrier trapping phenomena and the presence of surface trap states on the NCs.[59,60] In contrast, upon doping, a new NIR PL peak at 983 nm (1541 nm) emerged for the Yb^{3+} (Er^{3+})-doped LDP NCs (Figure 1C). These newly emerged NIR emission peaks correspond to the $^2F_{5/2}$−$^2F_{7/2}$ and $^4I_{13/2}$−$^4I_{15/2}$ electronic transitions within the $[YbCl_6]^{3-}$ and $[ErCl_6]^{3-}$ octahedral units, respectively.[61] PL excitation (PLE) spectra, monitored at the NIR PL peaks, matched well with the corresponding absorption profiles (Figure 1C), signifying an energy transfer process from the host $Cs_4CdSb_2Cl_{12}$ LDP NCs to the Ln^{3+} (i.e., Yb^{3+} or Er^{3+}) dopants. Time-resolved PL (TR-PL) spectroscopic measurements revealed an average PL decay lifetime (LT) of 1.15 ms for Yb-PL and 2.55 ms for Er-PL in the Ln^{3+}-doped LDP NCs (Figure 1D, Tables S4 and S5). Negligible changes were observed for the absorption spectra and XRD patterns of the Yb^{3+}- and Er^{3+}-doped $Cs_4CdSb_2Cl_{12}$ LDP NCs upon storage under ambient conditions (Figures S3 and S4). Additionally, the LDP crystal structure for Yb^{3+}- and Er^{3+}-doped $Cs_4CdSb_2Cl_{12}$ LDP NCs was maintained up to 150 °C (Figure S5), indicating their superior stability under both ambient and thermal conditions. Transmission electron microscopy (TEM) images showed spherical-like shapes with an average diameter of 21.2 ± 3.6, 21.9 ± 3.2, and 22.2 ± 2.9 nm for undoped, Yb^{3+}-doped, and Er^{3+}-doped $Cs_4CdSb_2Cl_{12}$ LDP NCs, respectively (Figure 1E−G). High-resolution TEM (HR-TEM) images displayed clear lattice fringes with a measured lattice d-spacing of 3.8 Å, corresponding to the (110) lattice planes viewed from the LDP [001] zone axis (Figure 1H−J). The corresponding fast Fourier transform (FFT) images matched the simulated electron diffraction patterns, further confirming the structure assignment of the trigonal LDP crystal phase (Figure 1H−J, Figure S1).

To investigate the Ln^{3+} doping effects on the optical properties and crystal structures of $Cs_4CdSb_2Cl_{12}$ LDP NCs,

https://doi.org/10.1021/jacs.3c11164
J. Am. Chem. Soc. 2024, 146, 3200−3209

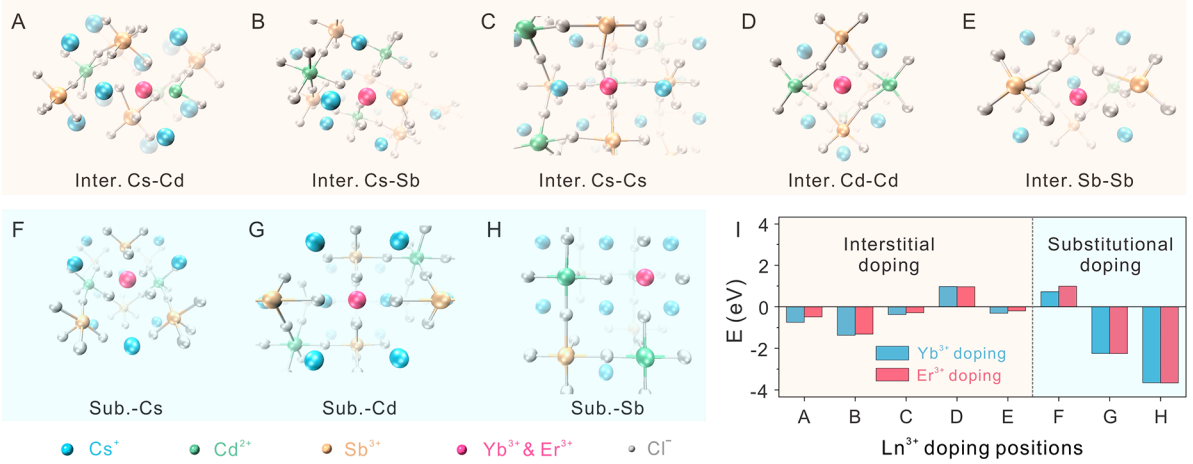

Figure 3. Optimized atomic configurations and the associated formation energies of various possible Yb^{3+} or Er^{3+} ion doping scenarios in $Cs_4CdSb_2Cl_{12}$ LDPs. (A–E) Different interstitial (Inter.) positions for the dopants between nearest Cs–Cd, Cs–Sb, Cs–Cs, Cd–Cd, and Sb–Sb atomic pairs. (F–H) Different substitution (Sub.) positions for the dopants replacing the Cs, Cd, or Sb site. (I) The calculated formation energies were obtained under different interstitial and substitutional doping conditions.

we synthesized a series of Ln^{3+} (Yb^{3+} or Er^{3+})-doped $Cs_4CdSb_2Cl_{12}$ LDP NCs with different doping concentrations (defined as the precursor feeding ratio of [Ln]/([Ln] + [Sb]; see SI for details) and conducted optical and structural characterizations (Figure 2). The lanthanide doping concentrations in the final LDP NCs are listed in Table S6. As shown in Figure 2A and D, all the Ln^{3+} (Yb^{3+} or Er^{3+})-doped $Cs_4CdSb_2Cl_{12}$ LDP NCs displayed similar absorption profiles with a slight decrease for bandgap (BG) values by Tauc plot analysis due to Ln^{3+} doping induced lattice expansion (Figures 2B,E and S6). However, as the Ln^{3+} doping concentration increased, the Ln-induced NIR PL peak intensity increased initially, reaching its maximum value at a Yb^{3+} (Er^{3+}) doping concentration of 20% (15%) before the subsequent PL intensity decreased (Figure 2C,F). While the initial increase in PL intensity can be explained by improved energy transfer efficiency from the host NC materials to the Ln^{3+} dopants and increased number of Ln-emitting sites (Figure 2K,L),[44] the subsequent intensity drop was mainly caused by the self-quenching effect resulting from inter-Ln^{3+} coupling and an increased presence of lattice defects as incorporating more Ln^{3+} dopant impurities (Figure 2C,F). The PL QYs for Ln^{3+} (Yb^{3+} or Er^{3+})-doped LDP NCs are listed in Table S7. In addition to the optical property changes, XRD measurements showed a well-preserved LDP structure in a trigonal phase for all of the Ln^{3+} (Yb^{3+} or Er^{3+})-doped $Cs_4CdSb_2Cl_{12}$ LDP NCs (Figure 2G–J). However, all of the Bragg diffraction peaks in the XRD patterns continuously shifted to smaller angles while increasing the Ln^{3+} doping concentration (Figure 2G–J). These results suggested a consistent lattice expansion of the LDP crystalline lattices upon doping increased amounts of large Ln^{3+} cations (doping concentration increased from 5% to 25%) (Figure S7), matching well with the evolution of bandgaps and their electronic structures (Figures 2B,E and S6).

To gain deeper insights into the detailed doping positions and associated doping mechanisms, we conducted DFT calculations to determine the formation energy and structural stability of various LDP lattice configurations incorporated with Yb^{3+} or Er^{3+} dopant ions (see SI for calculation details). First, to identify the Ln^{3+} doping position, we considered eight $Cs_4CdSb_2Cl_{12}$ LDP atomic lattice configurations, taking interstitial (five cases) and substitutional (three cases) Ln^{3+} doping scenarios into account (Figure 3A–H). These configurations were structurally relaxed and further optimized. The associated formation energies were calculated as shown in Figure 3I and Table S8 (more calculation details are discussed in the SI). The calculation results showed that Yb^{3+} or Er^{3+} ions exhibited similar doping behaviors due to their nearly identical ionic sizes and the same valence state and coordination environment. Among the interstitial doping scenarios, while doping at the Cd–Cd site resulted in a positive formation energy (thermodynamically unfavored) of 1.46 eV (for Yb^{3+} doping) or 1.44 eV (for Er^{3+} doping), all other interstitial doping scenarios led to negative formation energies (thermodynamically favored, Figure 3I). The unfavored inter-Cd doping position was possibly caused by the short distance between two neighboring Cd^{2+} ions (i.e., 7.48 Å, Figure S8) and a high electrostatic repulsion arising from the surrounding metal cations, compared to other interstitial doping sites. The lowest formation energies among all the interstitial Ln^{3+} doping scenarios were calculated to be −2.06 eV (for Yb^{3+} doping) and −1.98 eV (for Er^{3+} doping), both for the Cs–Sb interstitial doping scenario (Figure 3B,I). In the substitutional doping cases, replacing Cs^+ cations with Ln^{3+} dopants was determined to be the least thermodynamically favored doping position due to their large discrepancies in both the valence state and ionic radius (Cs^+: 167 pm) (Figure 3F,I). In contrast, both Cd- and Sb-substitutional cases were thermodynamically more favorable than any of the interstitial doping cases (Figure 3G–I). In particular, the Sb^{3+}-to-Ln^{3+} substitutional doping mechanism gave the most negative formation energy: −5.49 eV for Yb^{3+} doping and −5.50 eV for Er^{3+} doping, representing the most favorable doping position of all the cases calculated here. The preference of the Sb^{3+}-to-Ln^{3+} doping mechanism was consistent with isoelectronic doping, which does not introduce unbalanced charges into the LDP NCs or more crystalline defects/vacancies inside the LDP lattices.

Upon determining the precise dopant positions and obtaining the stable structural configurations, we carried out DFT calculations on the band structures and projected density of states (DOS) to further our understanding of the Ln^{3+} doping (i.e., Sb^{3+}-to-Ln^{3+} substitutional doping) effects on the

https://doi.org/10.1021/jacs.3c11164
J. Am. Chem. Soc. 2024, 146, 3200−3209

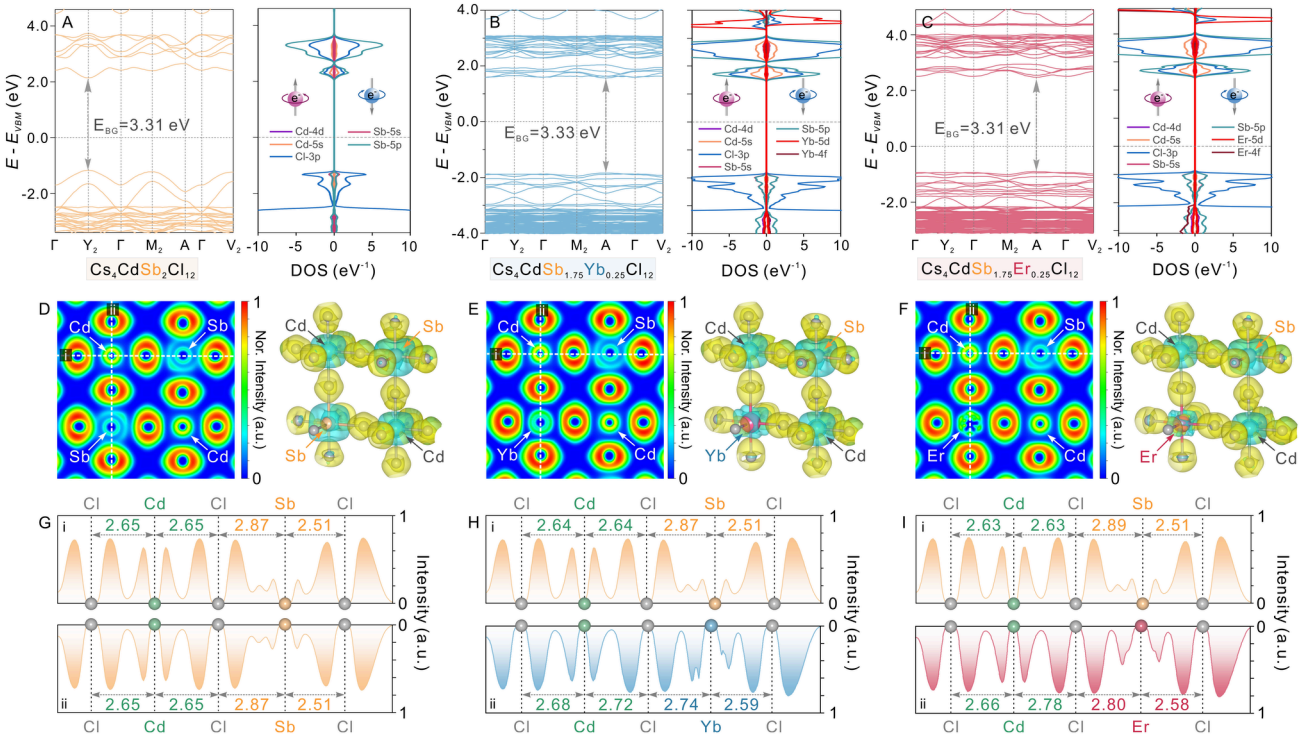

Figure 4. Electronic structures and electron localization function (ELF) of undoped and Yb^{3+}- and Er^{3+}-doped $Cs_4CdSb_2Cl_{12}$ LDPs. (A−C) Band structures (left panels) and projected density of states (DOS) diagrams (right panels) of undoped (A), Yb^{3+}-doped (B), and Er^{3+}-doped (C) $Cs_4CdSb_2Cl_{12}$ LDPs. The Fermi energy is indicated by the gray dashed lines. (D−F) ELF (left panels) profiles and charge density difference (right panels) of undoped (D), Yb^{3+}-doped (E), and Er^{3+}-doped (F) $Cs_4CdSb_2Cl_{12}$ LDPs. The colors in the ELF 2D mapping indicate the strength of the electron density. For charge density differences, the yellow and light blue surfaces represent the charge gain and charge loss, respectively. (G−I) 1D intensity profiles of undoped (G), Yb^{3+}-doped (H), and Er^{3+}-doped (I) $Cs_4CdSb_2Cl_{12}$ LDPs along two white dashed lines in the corresponding ELF 2D mapping (D−F, left panels), revealing the evolution of electron density distribution changes between Cd^{2+}, Sb^{3+}/Yb^{3+}/Er^{3+}, and Cl^- ions.

electronic structures of $Cs_4CdSb_2Cl_{12}$ LDPs (Figure 4, see the SI for detailed calculations). The calculation results showed that the undoped $Cs_4CdSb_2Cl_{12}$ LDP exhibited a direct bandgap of 3.31 eV with the conduction band minimum (CBM) and valence band maximum (VBM) located at the same "Y_2" high symmetry point (Figure 4A, left panel). The corresponding projected DOS revealed that the CBM was mostly contributed by Sb 5p, Cl 3p, and Cd 5s orbitals, while the VBM was mainly composed of Cl 3p, Sb 5s, and 5p orbitals (Figure 4A, right panel). After Yb^{3+} doping, the band structure preserved a similar direct bandgap of 3.33 eV (Figure 4B, left panel), with both CBM and VBM showing an additional small contribution from the Yb 5d orbital (Figure 4B, right panel). Furthermore, both the CBM and VBM shifted to the "A" high symmetry point, manifesting a symmetry change in the localized octahedral environment upon Ln^{3+} doping. Similarly, in the case of Er^{3+} doping, the band structure of the LDP was retained well with a direct bandgap of 3.31 eV (Figure 4C). Both CBM and VBM of the Er^{3+}-doped LDP were located at the "A" high symmetry point, where the CBM was mainly composed of Cl 3p, Sb 5p, and Cd 5s orbitals, while the VBM mostly consisted of Cl 3p, Sb 5s, and 5p orbitals, with a small contribution from Er 5d orbitals (Figure 4C). These calculation results implied that Ln^{3+} doping mainly introduced additional contributions from the Ln (Yb or Er) 5d orbitals to the VBM and CBM of the LDP host, with minimal effects on its bandgap structure nature.

Next, we conducted DFT calculations on the electron localization function (ELF) and charge density difference for the undoped and Ln^{3+}-doped (substituting Sb^{3+}) $Cs_4CdSb_2Cl_{12}$ LDPs to further investigate the influences of doping on the bond characteristics and charge distributions of the LDP host material (Figure 4D−F). In the case of undoped $Cs_4CdSb_2Cl_{12}$ LDP, the charge gain was distributed around Cl^- ions due to electron donations from Cd^{2+} or Sb^{3+} in the $[CdCl_6]^{4-}$ or $[SbCl_6]^{3-}$ octahedral units (Figure 4D, left panel). The associated 2D ELF mapping illustrated minimal electron densities between Cd^{2+} cations and Cl^- anions, suggesting an ionic Cd−Cl bond characteristic (Figure 4D, right panel). In comparison, the Sb−Cl bonds displayed an ionic bond characteristic, however, with a small contribution of covalent bonding feature attributable to the higher electronegtivity of the Sb atom than the Cd atom (Figure 4D, right panel). The corresponding 1D intensity profiles along the white dashed lines in Figure 4D further proved the same Cd−Cl bond strength with identical Cd−Cl bond length (2.65 Å) in the $[CdCl_6]^{4-}$ octahedral unit, while the $[SbCl_6]^{3-}$ octahedral unit exhibited certain distortion with different Sb−Cl bond lengths (i.e., 2.51 and 2.87 Å) (Figure 4G). Upon Ln^{3+} doping, the characteristic of Cd−Cl and Sb−Cl bonds presented negligible changes with no obvious charge redistribution between cations (i.e., Cd^{2+} or Sb^{3+}) and anions (i.e., Cl^-) (Figure 4E,F). The newly formed Yb−Cl and Er−Cl bonds exhibited an ionic bond characteristic with charge gain (loss) around Cl^- anions (Yb^{3+} or Er^{3+} cations), consistent with the ELF calculation results (Figure 4E,F). Within the LDP lattice, the dopant-involved octahedral units (i.e., $[YbCl_6]^{3-}$ and $[ErCl_6]^{3-}$ octahedra) showed obvious distortions with the Ln−Cl bonds along the Cd−Cl−Ln axis varied from 2.74 to 2.59 Å for the Yb^{3+} doping case (Figure

https://doi.org/10.1021/jacs.3c11164
J. Am. Chem. Soc. 2024, 146, 3200−3209

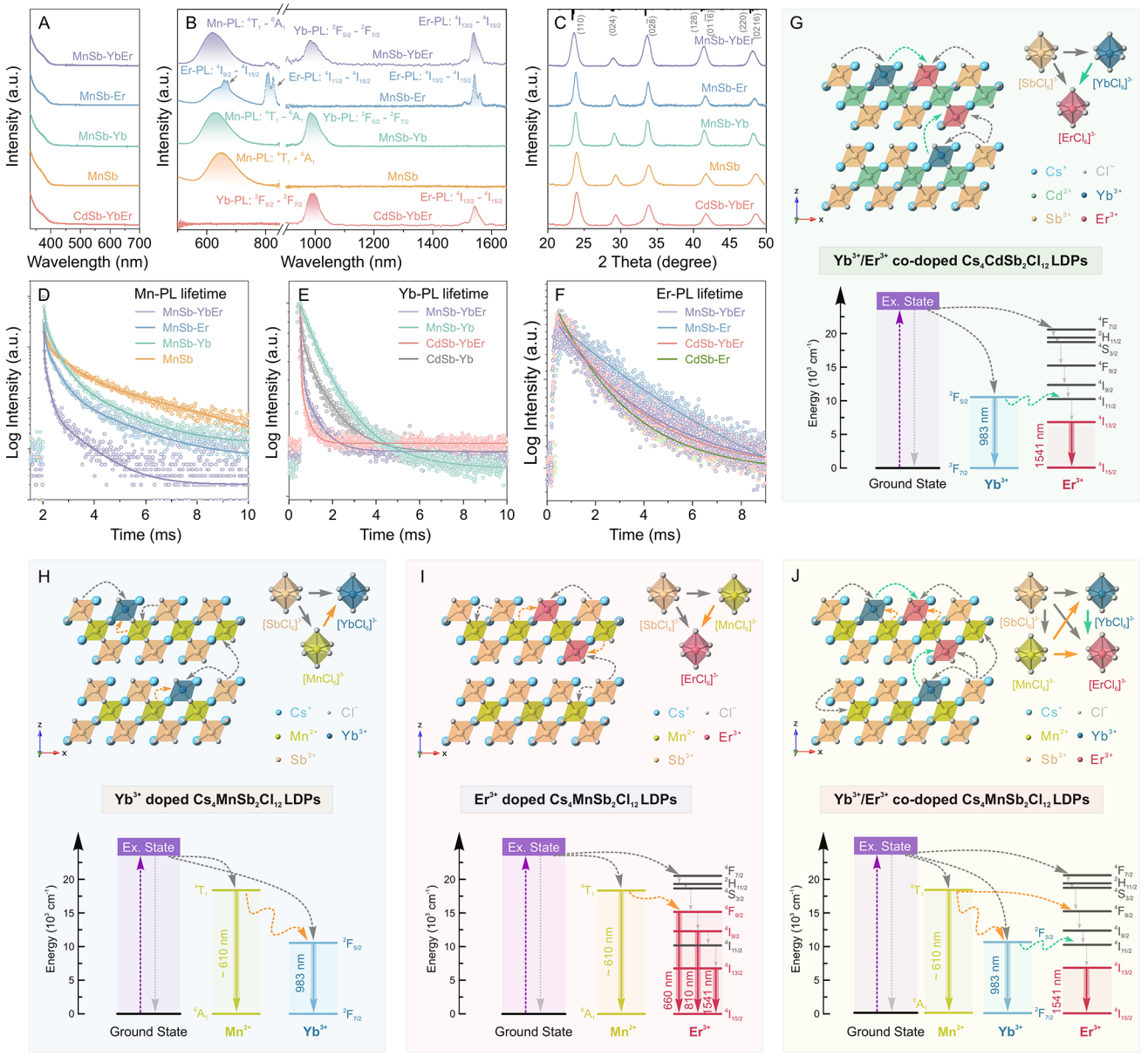

Figure 5. Sensitization effects of intermediate energy levels on the optical properties of Ln^{3+} (Yb^{3+}, Er^{3+})-doped $Cs_4M(II)Sb_2Cl_{12}$ (M(II): Cd^{2+}, Mn^{2+}) LDP NCs. (A) Absorption and (B) PL spectra, (C) XRD patterns of Yb^{3+}/Er^{3+}-co-doped $Cs_4CdSb_2Cl_{12}$ (CdSb-YbEr) LDP NCs, undoped (MnSb) and Yb^{3+}-doped (MnSb-Yb), Er^{3+}-doped (MnSb-Er), and Yb^{3+}/Er^{3+}-co-doped (MnSb-YbEr) $Cs_4MnSb_2Cl_{12}$ LDP NCs. (D−F) PL lifetime decays for Mn-PL (D), Yb-PL (E), and Er-PL (F) for different Ln^{3+} (Yb^{3+}, Er^{3+})-doped $Cs_4M(II)Sb_2Cl_{12}$ (M(II): Cd^{2+}, Mn^{2+}) LDP NCs when monitoring the Mn-PL at 630 nm and NIR PL at 983 and 1541 nm, respectively. (G−J) The schematics of the proposed energy transfer process of Yb^{3+}/Er^{3+}-co-doped $Cs_4CdSb_2Cl_{12}$ (G) and Yb^{3+}-doped (H), Er^{3+}-doped (I), and Yb^{3+}/Er^{3+}-co-doped (J) $Cs_4MnSb_2Cl_{12}$LDP NCs. Top panels show the atomic models; bottom panels exhibit the band alignment and electronic state energy levels for the LDP host and dopant ions, respectively.

4H) and from 2.80 to 2.58 Å for the Er^{3+} doping case (Figure 4I). In addition, the Ln^{3+} doping resulted in distortion of neighboring $[CdCl_6]^{4-}$ octahedra with elongated Cd−Cl bond lengths only along the Cd−Cl−Ln direction (Figure 4H,I). A slightly higher degree of $[CdCl_6]^{4-}$ octahedral distortion for the Er^{3+}-doped $Cs_4CdSb_2Cl_{12}$ LDP can be explained by the larger ionic size of the Er^{3+} ion as compared to the Yb^{3+} ion (Figure 4H,I). This supports that Ln^{3+} doping in $Cs_4CdSb_2Cl_{12}$ LDPs leads to a reduction in the local site symmetry of $[CdCl_6]^{4-}$ to C_{4v} compared to their high O_h symmetry in the undoped $Cs_4CdSb_2Cl_{12}$ LDPs. This local site symmetry breakdown induced by Ln^{3+} doping enhances the absorption and excitation of host materials and thereby promotes the energy transfer process for the observed NIR emissions.[47,62]

Co-doping different types of impurity ions into perovskite NCs is an effective means to gain deeper understandings of multi-dopant-induced bandgap engineering and energy transfer processes within the system.[43,63] Especially, with suitable energy level alignments of the host perovskite NCs and different dopants, intermediate-sensitization-assisted host-to-dopant and interdopant energy transfer processes may synergistically occur, leading to novel and unique optical properties of the co-doped perovskite NCs.[42,43,64] To explore this effect, we synthesized Yb^{3+}/Er^{3+} co-doped $Cs_4CdSb_2Cl_{12}$ LDP NCs with the same doping concentration of 15% for both

https://doi.org/10.1021/jacs.3c11164
J. Am. Chem. Soc. 2024, 146, 3200−3209

Yb^{3+} and Er^{3+} ions (see synthetic details in the SI). The absorption spectrum of the resulting sample displayed a slightly red-shifted band edge absorption with a reduced bandgap around 3.139 eV compared to the undoped or single-type Ln^{3+}-doped LDP host NCs (Figures 5A, S9). However, the co-doped LDP NCs exhibited a dual-wavelength PL emission profile covering both NIR-I (i.e., 983 nm, $^2F_{5/2}-^2F_{7/2}$ transition of Yb^{3+} ions) and NIR-II (i.e., 1541 nm, $^4I_{13/2}-^4I_{15/2}$ transition of Er^{3+} ions) windows (Figure 5B). XRD measurements showed the same LDP phase, confirming the crystal structural preservation of the host LDP NCs upon co-doping with Yb^{3+} and Er^{3+} ions (Figure 5C). PLE spectra, when monitoring both Yb-PL and Er-PL, aligned well with the absorption profile, indicating that the dual-wavelength PL originated from the energy transfer from the LDP NC host to two different dopants (Figure S10). TR-PL measurements were then conducted to probe the detailed energy transfer processes of the NCs (Figure 5D−F). In comparison to the single-type Ln^{3+} (either Yb^{3+} or Er^{3+})-doped $Cs_4CdSb_2Cl_{12}$ LDP NCs, we observed a shortening of the Yb-PL LT from 1.15 ms to 0.38 ms and a lengthening of the Er-PL LT from 2.55 ms to 2.99 ms in the Yb^{3+}/Er^{3+}-co-doped $Cs_4CdSb_2Cl_{12}$ LDP NCs (Figure 5E,F and Tables S4, S5). These results suggested the occurrence of interdopant energy transfer from the $^2F_{5/2}$ state (depopulated state) of the Yb^{3+} ions to the populated state of the neighboring Er^{3+} ions in the LDP lattices, resulting in the shortened (prolonged) LT of the Yb-PL (Er-PL) (Figure 5G).[43,64]

To further investigate the impact of the LDP NC host on the optical properties of the Ln^{3+} dopants, we selected $Cs_4MnSb_2Cl_{12}$ LDP NCs as the host material for Ln^{3+} doping.[65] The intrinsic emission from the d−d transition of Mn^{2+} ions provides an opportunity to explore intermediate-sensitization-assisted energy transfer processes upon Ln^{3+} doping. We thus synthesized undoped $Cs_4MnSb_2Cl_{12}$ LDP NCs, as well as $Cs_4MnSb_2Cl_{12}$ LDP NCs doped with Yb^{3+}, Er^{3+}, or Yb^{3+}/Er^{3+} ions using the hot-injection method as described earlier (see SI for synthetic details).[55,56] The synthesized $Cs_4MnSb_2Cl_{12}$ LDP NCs showed an absorption band edge at around 390 nm with a direct bandgap of 3.195 eV through Tauc plot analysis (Figures 5A, S9). These NCs shared the same LDP crystal structure with a trigonal phase as that of $Cs_4CdSb_2Cl_{12}$ LDP NCs (Figure S11). An intrinsic emission peak centered at 648 nm, arising from the energy transfer associated with $^4T_1-^6A_1$ d−d transition of Mn^{2+} ions, was measured with a characteristic Mn-PL LT of 2.25 ms (Figure 5D and Table S9).[43,66] Upon doping with Ln^{3+} ions (i.e., Yb^{3+}, Er^{3+}, or both), neither the bandgap nor the crystal structure showed an obvious change when compared to the undoped LDP host NCs (Figures 5A,C and S9). However, additional emission features emerged following doping (Figure 5B). In the case of Yb^{3+}-doped $Cs_4MnSb_2Cl_{12}$ LDP NCs, the characteristic Yb-PL peak at 983 nm ($^2F_{5/2}-^2F_{7/2}$ transition of the Yb^{3+} ions) showed up, alongside the pristine Mn-PL peak (Figure 5B). The Mn-PL decay LT shortened to 0.74 ms from the 2.25 ms of undoped $Cs_4MnSb_2Cl_{12}$ LDP NCs, while the Yb-PL decay LT extended to 1.47 ms compared to 1.15 ms of the Yb^{3+}-doped $Cs_4CdSb_2Cl_{12}$ LDP NCs (Figure 5D,E, and Tables S4, S9). These changes indicated the occurrence of energy transfer from the $^4T_1$ state (depopulated state) of Mn^{2+} ions to the $^2F_{5/2}$ state (populated state) of Yb^{3+} dopants in the LDP NCs (Figure 5H).[43,64] Similarly, the Er-PL feature at 1541 nm ($^4I_{13/2}-^4I_{15/2}$ transition of the Er^{3+} ions) emerged upon doping Er^{3+} ions into the $Cs_4MnSb_2Cl_{12}$ LDP NC host (Figure 5B). Remarkably, two additional sharp emission bands at 660 and 810 nm can be clearly visualized in the PL spectrum, corresponding to the $^4F_{9/2}-^4I_{15/2}$ and $^4I_{9/2}-^4I_{15/2}$ electronic transitions of Er^{3+} ions in an octahedral coordination environment, respectively (Figure 5B and Figure S10). It is noteworthy that these new emission bands were not observed when using $Cs_4CdSb_2Cl_{12}$ LDP NCs as the host material with either Er^{3+} doping or Yb^{3+}/Er^{3+} co-doping (Figures 1C, 2B, and 2D). These differences in PL profiles led to a reasonable hypothesis: the presence of nearby Mn^{2+} ion centers enabled an energy transfer pathway from the Mn^{2+} excited state ($^4T_1$ state) to the predark states ($^4F_{9/2}$ and $^4I_{9/2}$ states) of Er^{3+} ion dopants owing to the proximity of these energy levels and their spin-allowed transition nature (identical spin multiplicity, i.e., 4) (Figure 5I).[67,68] Moreover, this hypothesis was supported by the significantly shortened Mn-PL LT (0.54 ms) compared to that of the undoped counterpart (Mn-PL LT of 2.25 ms) (Figure 5D). Furthermore, the prolonged Er-PL LT at 1541 nm (7.84 ms) suggested a possible energy transfer from the Mn^{2+} ions of the host NCs to the nearby Er^{3+} ion dopants (Figure 5F), further confirming that the Mn component can act as an intermediate energy sensitizer in the Ln^{3+}-doped $Cs_4MnSb_2Cl_{12}$ LDP NCs (Figure 5I). It is worth noting that our study represents the first observation of brightening the $^4F_{9/2}$ and $^4I_{9/2}$ electronic states of Er^{3+} ions in colloidal perovskite NCs through the energy sensitization of Mn^{2+} ions, marking a rare example of brightening predark states of Er^{3+} ions.

When co-doping both Yb^{3+} and Er^{3+} ions into the $Cs_4MnSb_2Cl_{12}$ LDP NC host, we achieved a triple-wavelength emission profile with three PL peaks located in the visible (618 nm for Mn-PL), NIR-I (983 nm for Yb-PL), and NIR-II (1541 nm for Er-PL) regions (Figure 5B). In addition to direct energy transfer from the $Cs_4MnSb_2Cl_{12}$ LDP NC host to Yb^{3+} and Er^{3+} ion dopants, we proposed that both Mn^{2+} and Yb^{3+} ion centers acted as intermediate energy sensitizers, allowing for a stepwise energy transfer process from the populated $^4T_1$ electronic state of Mn^{2+} ions to the $^4F_{5/2}$ electronic state of Yb^{3+} ions and then to the $^4I_{13/2}$ state of Er^{3+} ions (Figure 5J). These energy transfer processes were confirmed through the TR-PL measurements, which showed shortened Mn-PL (0.31 ms) and Yb-PL LTs (0.65 ms) and a lengthened Er-PL LT (3.40 ms) compared with those of undoped $Cs_4MnSb_2Cl_{12}$ LDP NCs, Yb^{3+}-only-doped $Cs_4MnSb_2Cl_{12}$ LDP NCs, and Er^{3+}-only-doped $Cs_4CdSb_2Cl_{12}$ LDP NCs, respectively. Notably, the absence of the two additional Er-PL emission bands at 660 and 810 nm indicated that the corresponding energy transfer pathways were blocked from the $^4T_1$ excited state of Mn^{2+} ions in the host LDP NCs to the $^4F_{9/2}$ and $^4I_{9/2}$ states of Er^{3+} ion dopants due to the presence of a competing energy relaxation channel to the $^4F_{5/2}$ electronic state of Yb^{3+} ion dopants (Figure 5J).

CONCLUSION

In conclusion, we have successfully synthesized colloidal rare earth Ln^{3+} (Yb^{3+} or Er^{3+}, or both)-doped $Cs_4M(II)Sb_2Cl_{12}$ (M(II): Cd or Mn) LDP NCs with controlled doping concentrations using a hot-injection approach. The obtained samples showed excellent LDP crystallinity with a trigonal phase and featured newly emerged NIR emission bands attributed to energy transfer from the LDP NC host to the Ln^{3+} dopants. Detailed DFT calculations unveiled that the

https://doi.org/10.1021/jacs.3c11164
J. Am. Chem. Soc. 2024, 146, 3200−3209

thermodynamically favored doping mechanisms involved the substitution of Sb^{3+} cations with Ln^{3+} (Yb^{3+} or Er^{3+}) dopants within the LDP lattices while maintaining the overall charge neutrality and structural stability of the NCs. Moreover, our study showcased that through incorporating both Yb^{3+} and Er^{3+} dopants and introducing the Mn^{2+} component into the host LDP NCs, the pathways for host-to-dopant and interdopant energy transfers can be facilitated by means of intermediate energy sensitization processes. Notably, we demonstrated the first example of precise control over the activation and deactivation of two predark electronic states (specifically, the $^4F_{9/2}$ and $^4I_{9/2}$ states) of Er^{3+} ion dopants through deliberate compositional tuning of the LDP NCs. We envision that our research findings can serve as a catalyst for the exploration of novel doping systems and the development of colloidal lead-free perovskite nanomaterials, ultimately fueling advancements in a wide spectrum of optoelectronic applications.

■ ASSOCIATED CONTENT

Supporting Information

The Supporting Information is available free of charge at https://pubs.acs.org/doi/10.1021/jacs.3c11164.

Additional experimental details, DFT calculation details, XRD, lifetime, PLE analyses, and Tauc plots (PDF)

■ AUTHOR INFORMATION

Corresponding Authors

Xinzhong Wang − *Institute of Information Technology, Shenzhen Institute of Information Technology, Shenzhen 518172, China*; Email: wangxz@sziit.edu.cn

Ou Chen − *Department of Chemistry, Brown University, Providence, Rhode Island 02912, United States*; orcid.org/0000-0003-0551-090X; Email: ouchen@brown.edu

Authors

Tong Cai − *Department of Chemistry, Brown University, Providence, Rhode Island 02912, United States;* Present Address: Department of Chemistry, Northwestern University, Evanston, Illinois 60201, United States

Wenwu Shi − *Department of Chemistry, Brown University, Providence, Rhode Island 02912, United States; Institute of Information Technology, Shenzhen Institute of Information Technology, Shenzhen 518172, China;* Present Address: School of Physical Science and Technology, Southwest University, Chongqing 400715, China.

Rongzhen Wu − *Department of Chemistry, Brown University, Providence, Rhode Island 02912, United States*

Chun Chu − *Department of Chemistry, Syracuse University, Syracuse, New York 13244, United States*

Na Jin − *Department of Chemistry, Brown University, Providence, Rhode Island 02912, United States*

Junyu Wang − *Department of Chemistry, Brown University, Providence, Rhode Island 02912, United States*

Weiwei Zheng − *Department of Chemistry, Syracuse University, Syracuse, New York 13244, United States*; orcid.org/0000-0003-1394-1806

Complete contact information is available at: https://pubs.acs.org/10.1021/jacs.3c11164

Author Contributions

T.C. and W.S. contributed equally.

Notes

The authors declare no competing financial interest.

■ ACKNOWLEDGMENTS

O.C. acknowledges support from Brown University startup funds. TEM and XRD measurements were performed at the Electron Microscopy Facility in the Institute for Molecular and Nanoscale Innovation (IMNI) at Brown University.

■ REFERENCES

(1) Dey, A.; Ye, J.; De, A.; Debroye, E.; Ha, S. K.; Bladt, E.; Kshirsagar, A. S.; Wang, Z.; Yin, J.; Wang, Y.; Quan, L. N.; Yan, F.; Gao, M.; Li, X.; Shamsi, J.; Debnath, T.; Cao, M.; Scheel, M. A.; Kumar, S.; Steele, J. A.; Gerhard, M.; Chouhan, L.; Xu, K.; Wu, X. G.; Li, Y.; Zhang, Y.; Dutta, A.; Han, C.; Vincon, I.; Rogach, A. L.; Nag, A.; Samanta, A.; Korgel, B. A.; Shih, C. J.; Gamelin, D. R.; Son, D. H.; Zeng, H.; Zhong, H.; Sun, H.; Demir, H. V.; Scheblykin, I. G.; Mora-Sero, I.; Stolarczyk, J. K.; Zhang, J. Z.; Feldmann, J.; Hofkens, J.; Luther, J. M.; Perez-Prieto, J.; Li, L.; Manna, L.; Bodnarchuk, M. I.; Kovalenko, M. V.; Roeffaers, M. B. J.; Pradhan, N.; Mohammed, O. F.; Bakr, O. M.; Yang, P.; Muller-Buschbaum, P.; Kamat, P. V.; Bao, Q.; Zhang, Q.; Krahne, R.; Galian, R. E.; Stranks, S. D.; Bals, S.; Biju, V.; Tisdale, W. A.; Yan, Y.; Hoye, R. L. Z.; Polavarapu, L. State of the Art and Prospects for Halide Perovskite Nanocrystals. *ACS Nano* **2021**, *15* (7), 10775−10981.

(2) Shamsi, J.; Urban, A. S.; Imran, M.; De Trizio, L.; Manna, L. Metal Halide Perovskite Nanocrystals: Synthesis, Post-Synthesis Modifications, and Their Optical Properties. *Chem. Rev.* **2019**, *119* (5), 3296−3348.

(3) Protesescu, L.; Yakunin, S.; Bodnarchuk, M. I.; Krieg, F.; Caputo, R.; Hendon, C. H.; Yang, R. X.; Walsh, A.; Kovalenko, M. V. Nanocrystals of Cesium Lead Halide Perovskites ($CsPbX_3$, X = Cl, Br, and I): Novel Optoelectronic Materials Showing Bright Emission with Wide Color Gamut. *Nano Lett.* **2015**, *15* (6), 3692−6.

(4) Nagaoka, Y.; Hills-Kimball, K.; Tan, R.; Li, R.; Wang, Z.; Chen, O. Nanocube Superlattices of Cesium Lead Bromide Perovskites and Pressure-Induced Phase Transformations at Atomic and Mesoscale Levels. *Adv. Mater.* **2017**, *29* (18), No. 1606666.

(5) Hills-Kimball, K.; Yang, H.; Cai, T.; Wang, J.; Chen, O. Recent Advances in Ligand Design and Engineering in Lead Halide Perovskite Nanocrystals. *Adv. Sci.* **2021**, *8* (12), No. 2100214.

(6) Dedecker, K.; Grancini, G. Dealing with Lead in Hybrid Perovskite: A Challenge to Tackle for a Bright Future of This Technology? *Adv. Energy Mater.* **2020**, *10*, No. 2001471.

(7) Giustino, F.; Snaith, H. J. Toward Lead-Free Perovskite Solar Cells. *ACS Energy Lett.* **2016**, *1* (6), 1233−1240.

(8) Ning, W.; Gao, F. Structural and Functional Diversity in Lead-Free Halide Perovskite Materials. *Adv. Mater.* **2019**, *31* (22), No. 1900326.

(9) Cai, T.; Dube, L.; Saghy, P.; Yang, H.; Chen, O. Progress in All-inorganic Heterometallic Halide Layered Double Perovskites. *Trends Chem.* **2023**, *5* (1), 29−449.

(10) Li, Q.; Chen, Z.; Yang, B.; Tan, L.; Xu, B.; Han, J.; Zhao, Y.; Tang, J.; Quan, Z. Pressure-Induced Remarkable Enhancement of Self-Trapped Exciton Emission in One-Dimensional $CsCu_2I_3$ with Tetrahedral Units. *J. Am. Chem. Soc.* **2020**, *142* (4), 1786−1791.

(11) Zhang, L.; Wang, K.; Zou, B. Bismuth Halide Perovskite-Like Materials: Current Opportunities and Challenges. *ChemSusChem* **2019**, *12* (8), 1612−1630.

(12) Creutz, S. E.; Liu, H.; Kaiser, M. E.; Li, X.; Gamelin, D. R. Structural Diversity in Cesium Bismuth Halide Nanocrystals. *Chem. Mater.* **2019**, *31* (13), 4685−4697.

(13) Pal, J.; Manna, S.; Mondal, A.; Das, S.; Adarsh, K. V.; Nag, A. Colloidal Synthesis and Photophysics of $M_3Sb_2I_9$ (M = Cs and Rb)

Nanocrystals: Lead-Free Perovskites. *Angew. Chem., Int. Ed. Engl.* **2017**, *56* (45), 14187−14191.
(14) Yang, H.; Cai, T.; Liu, E.; Hills-Kimball, K.; Gao, J.; Chen, O. Synthesis and Transformation of Zero-Dimensional Cs_3BiX_6 (X = Cl, Br) Perovskite-Analogue Nanocrystals. *Nano Res.* **2020**, *13* (1), 282−291.
(15) Pradhan, B.; Kumar, G. S.; Sain, S.; Dalui, A.; Ghorai, U. K.; Pradhan, S. K.; Acharya, S. Size Tunable Cesium Antimony Chloride Perovskite Nanowires and Nanorods. *Chem. Mater.* **2018**, *30* (6), 2135−2142.
(16) Zhang, R.; Wang, Z.; Xu, X.; Mao, X.; Xiong, J.; Yang, Y.; Han, K. All-Inorganic Rare-Earth Halide Double Perovskite Single Crystals with Highly Efficient Photoluminescence. *Add. Opt. Mater.* **2021**, *9* (19), No. 2100689.
(17) Du, K. Z.; Meng, W.; Wang, X.; Yan, Y.; Mitzi, D. B. Bandgap Engineering of Lead-Free Double Perovskite $Cs_2AgBiBr_6$ through Trivalent Metal Alloying. *Angew. Chem., Int. Ed. Engl.* **2017**, *56* (28), 8158−8162.
(18) Liu, Y.; Nag, A.; Manna, L.; Xia, Z. Lead-Free Double Perovskite $Cs_2AgInCl_6$. *Angew. Chem., Int. Ed. Engl.* **2021**, *60* (21), 11592−11603.
(19) Slavney, A. H.; Leppert, L.; Saldivar Valdes, A.; Bartesaghi, D.; Savenije, T. J.; Neaton, J. B.; Karunadasa, H. I. Small-Band-Gap Halide Double Perovskites. *Angew. Chem., Int. Ed. Engl.* **2018**, *57* (39), 12765−12770.
(20) Karmakar, A.; Dodd, M. S.; Agnihotri, S.; Ravera, E.; Michaelis, V. K. Cu(II)-Doped $Cs_2SbAgCl_6$ Double Perovskite: A Lead-Free, Low-Bandgap Material. *Chem. Mater.* **2018**, *30* (22), 8280−8290.
(21) Majher, J. D.; Gray, M. B.; Strom, T. A.; Woodward, P. M. $Cs_2NaBiCl_6$:Mn^{2+}—A New Orange-Red Halide Double Perovskite Phosphor. *Chem. Mater.* **2019**, *31* (5), 1738−1744.
(22) Manna, D.; Das, T. K.; Yella, A. Tunable and Stable White Light Emission in Bi^{3+}-Alloyed $Cs_2AgInCl_6$ Double Perovskite Nanocrystals. *Chem. Mater.* **2019**, *31* (24), 10063−10070.
(23) Dube, L.; Saghy, P.; Chen, O. Post-Synthetic Doping and Ligand Engineering of $Cs_2AgInCl_6$ Double Perovskite Nanocrystals. *J. Phys. Chem. C* **2023**, *127* (44), 21849−21859.
(24) Vargas, B.; Ramos, E.; Perez-Gutierrez, E.; Alonso, J. C.; Solis-Ibarra, D. A Direct Bandgap Copper-Antimony Halide Perovskite. *J. Am. Chem. Soc.* **2017**, *139* (27), 9116−9119.
(25) Singhal, N.; Chakraborty, R.; Ghosh, P.; Nag, A. Low-Bandgap $Cs_4CuSb_2Cl_{12}$ Layered Double Perovskite: Synthesis, Reversible Thermal Changes, and Magnetic Interaction. *Chem. Asian. J.* **2018**, *13*, 2085.
(26) Gray, M. B.; Majher, J. D.; Holzapfel, N. P.; Woodward, P. M. Exploring the Stability of Mixed-Halide Vacancy-Ordered Quadruple Perovskites. *Chem. Mater.* **2021**, *33* (6), 2165−2172.
(27) Lin, Y. P.; Hu, S.; Xia, B.; Fan, K. Q.; Gong, L. K.; Kong, J. T.; Huang, X. Y.; Xiao, Z.; Du, K. Z. Material Design and Optoelectronic Properties of Three-Dimensional Quadruple Perovskite Halides. *J. Phys. Chem. Lett.* **2019**, *10* (17), 5219−5225.
(28) Liu, M.; Matta, S. K.; Ali-Loytty, H.; Matuhina, A.; Grandhi, G. K.; Lahtonen, K.; Russo, S. P.; Vivo, P. Moisture-Assisted near-UV Emission Enhancement of Lead-Free $Cs_4CuIn_2Cl_{12}$ Double Perovskite Nanocrystals. *Nano Lett.* **2022**, *22* (1), 311−318.
(29) Wei, J.-H.; Liao, J.-F.; Wang, X.-D.; Zhou, L.; Jiang, Y.; Kuang, D.-B. All-Inorganic Lead-Free Heterometallic $Cs_4MnBi_2Cl_{12}$ Perovskite Single Crystal with Highly Efficient Orange Emission. *Matter* **2020**, *3* (3), 892−903.
(30) Mai, H.; Li, X.; Lu, J.; Wen, X.; Le, T. C.; Russo, S. P.; Chen, D.; Caruso, R. A. Synthesis of Layered Lead-Free Perovskite Nanocrystals with Precise Size and Shape Control and Their Photocatalytic Activity. *J. Am. Chem. Soc.* **2023**, *145* (31), 17337−17350.
(31) Yang, H.; Shi, W.; Nagaoka, Y.; Liu, Z.; Li, R.; Chen, O. Access and Capture of Layered Double Perovskite Polytypic Phase through High-Pressure Engineering. *J. Phys. Chem. C* **2023**, *127* (5), 2407−2415.
(32) Vargas, B.; Rodríguez-López, G.; Solis-Ibarra, D. The Emergence of Halide Layered Double Perovskites. *ACS Energy Lett.* **2020**, *5* (11), 3591−3608.
(33) Yang, H.; Cai, T.; Dube, L.; Chen, O. Synthesis of Double Perovskite and Quadruple Perovskite Nanocrystals through Post-Synthetic Transformation Reactions. *Chem. Sci.* **2022**, *13* (17), 4874−4883.
(34) Holzapfel, N. P.; Majher, J. D.; Strom, T. A.; Moore, C. E.; Woodward, P. M. $Cs_4Cd_{1-x}Mn_xBi_2Cl_{12}$—A Vacancy-Ordered Halide Perovskite Phosphor with High-Efficiency Orange-Red Emission. *Chem. Mater.* **2020**, *32* (8), 3510−3516.
(35) Lu, C. H.; Biesold-McGee, G. V.; Liu, Y.; Kang, Z.; Lin, Z. Doping and Ion Substitution in Colloidal Metal Halide Perovskite Nanocrystals. *Chem. Soc. Rev.* **2020**, *49* (14), 4953−5007.
(36) Zhang, Z.; Skripka, A.; Dahl, J. C.; Dun, C.; Urban, J. J.; Jaque, D.; Schuck, P. J.; Cohen, B. E.; Chan, E. M. Tuning Phonon Energies in Lanthanide-doped Potassium Lead Halide Nanocrystals for Enhanced Nonlinearity and Upconversion. *Angew. Chem., Int. Ed. Engl.* **2023**, *62* (1), No. 202212549.
(37) Stroyuk, O.; Raievska, O.; Hauch, J.; Brabec, C. J. Doping/Alloying Pathways to Lead-Free Halide Perovskites with Ultimate Photoluminescence Quantum Yields. *Angew. Chem., Int. Ed. Engl.* **2023**, *62* (3), No. 202212668.
(38) Zhang, L.; Yuan, M. Lanthanide Doped Lead-free Double Perovskites as the Promising Next Generation Ultra-broadband Light Sources. *Light Sci. Appl.* **2022**, *11* (1), 99.
(39) Yu, Y. J.; Zou, C.; Shen, W. S.; Zheng, X.; Tian, Q. S.; Yu, Y. J.; Chen, C. H.; Zhao, B.; Wang, Z. K.; Di, D.; Bakr, O. M.; Liao, L. S. Efficient Near-Infrared Electroluminescence from Lanthanide-Doped Perovskite Quantum Cutters. *Angew. Chem., Int. Ed. Engl.* **2023**, *62* (22), No. 202302005.
(40) Mir, W. J.; Sheikh, T.; Arfin, H.; Xia, Z.; Nag, A. Lanthanide Doping in Metal Halide Perovskite Nanocrystals: Spectral Shifting, Quantum Cutting and Optoelectronic Applications. *NPG Asia Mater.* **2020**, *12* (1), 9.
(41) Zeng, Z.; Xu, Y.; Zhang, Z.; Gao, Z.; Luo, M.; Yin, Z.; Zhang, C.; Xu, J.; Huang, B.; Luo, F.; Du, Y.; Yan, C. Rare-Earth-Containing Perovskite Nanomaterials: Design, Synthesis, Properties and Applications. *Chem. Soc. Rev.* **2020**, *49*, 1109−1143.
(42) Saghy, P.; Brown, A. M.; Chu, C.; Dube, L. C.; Zheng, W.; Robinson, J. R.; Chen, O. Lanthanide Double Perovskite Nanocrystals with Emissions Covering the UV-C to NIR Spectral Range. *Adv. Opt. Mater.* **2023**, *11* (12), No. 2300227.
(43) Cai, T.; Wang, J.; Li, W.; Hills-Kimball, K.; Yang, H.; Nagaoka, Y.; Yuan, Y.; Zia, R.; Chen, O. Mn^{2+}/Yb^{3+} Codoped $CsPbCl_3$ Perovskite Nanocrystals with Triple-Wavelength Emission for Luminescent Solar Concentrators. *Adv. Sci.* **2020**, *7* (18), No. 2001317.
(44) Milstein, T. J.; Kroupa, D. M.; Gamelin, D. R. Picosecond Quantum Cutting Generates Photoluminescence Quantum Yields Over 100% in Ytterbium-Doped $CsPbCl_3$ Nanocrystals. *Nano Lett.* **2018**, *18* (6), 3792−3799.
(45) Pan, G.; Bai, X.; Yang, D.; Chen, X.; Jing, P.; Qu, S.; Zhang, L.; Zhou, D.; Zhu, J.; Xu, W.; Dong, B.; Song, H. Doping Lanthanide into Perovskite Nanocrystals: Highly Improved and Expanded Optical Properties. *Nano Lett.* **2017**, *17* (12), 8005−8011.
(46) Chen, N.; Cai, T.; Li, W.; Hills-Kimball, K.; Yang, H.; Que, M.; Nagaoka, Y.; Liu, Z.; Yang, D.; Dong, A.; Xu, C. Y.; Zia, R.; Chen, O. Yb- and Mn-Doped Lead-Free Double Perovskite Cs_2AgBiX_6 (X = Cl^-, Br^-) Nanocrystals. *ACS Appl. Mater. Interfaces* **2019**, *11* (18), 16855−16863.
(47) Li, X.; Shen, X.; Lu, M.; Wu, J.; Zhong, Y.; Wu, Z.; Yu, W. W.; Gao, Y.; Hu, J.; Zhu, J.; Zhang, Y.; Bai, X. Wide-coverage and Efficient NIR Emission from Single-component Nanophosphors through Shaping Multiple Metal-halide Packages. *Angew. Chem., Int. Ed. Engl.* **2023**, *62* (14), No. 202217832.
(48) Liu, Y.; Rong, X.; Li, M.; Molokeev, M. S.; Zhao, J.; Xia, Z. Incorporating Rare-Earth Terbium(III) Ions into $Cs_2AgInCl_6$:Bi

https://doi.org/10.1021/jacs.3c11164
J. Am. Chem. Soc. 2024, 146, 3200−3209

Nanocrystals toward Tunable Photoluminescence. *Angew. Chem., Int. Ed. Engl.* **2020**, *59* (28), 11634−11640.
(49) Wang, S.; Qi, J.; Kershaw, S. V.; Rogach, A. L. Co-Doping of Cerium and Bismuth into Lead-Free Double Perovskite $Cs_2AgInCl_6$ Nanocrystals Results in Improved Photoluminescence Efficiency. *ACS Nanosci. Au* **2022**, *2* (2), 93−101.
(50) Rachna; Singh, A.; Lamba, R. S.; Kumar, S.; Sapra, S. Self-Trapped Excitons Mediated Energy Transfer to Sm^{3+} in $Cs_2AgIn_{1-x}Sm_xCl_6$:Bi Double Perovskite Nanocrystals. *J. Phys. Chem. C* **2023**, *127* (1), 468−475.
(51) Zhao, J.; Pan, G.; Zhu, Y.; Liu, K.; You, W.; Chen, X.; Song, H.; Mao, Y. High-Efficiency and Wavelength-Tunable Near-Infrared Emission of Lanthanide Ions Doped Lead-Free Halide Double Perovskite Nanocrystals toward Fluorescence Imaging. *ACS Appl. Mater. & Interfaces* **2022**, *14* (37), 42215−42222.
(52) Yang, W.; Dang, P.; Zhang, G.; Lian, H.; Cheng, Z.; Li, G.; Lin, J. Mn^{2+} as an "Optical Energy Shutter" to Regulate Red-to-NIR Luminescence in Rare Earth Doped Layered Quadruple Perovskites. *Adv. Opt. Mater.* **2023**, *11*, No. 2300468.
(53) Dang, P.; Zhang, G.; Yang, W.; Lian, H.; Li, G.; Lin, J. Red−NIR Luminescence in Rare-Earth and Manganese Ions Codoped $Cs_4CdBi_2Cl_{12}$ Vacancy-Ordered Quadruple Perovskites. *Chem. Mater.* **2023**, *35* (4), 1640−1650.
(54) Li, J.; Xiao, J.; Lin, T.; Yan, Z.; Han, X. Lanthanide doping enabled multimodal luminescence in layered lead-free double perovskite $Cs_4MnBi_2Cl_{12}$. *J. Mater. Chem. C* **2022**, *10* (19), 7626−7632.
(55) Cai, T.; Shi, W.; Gosztola, D. J.; Kobbekaduwa, K.; Yang, H.; Jin, N.; Nagaoka, Y.; Dube, L.; Schneider, J.; Hwang, S.; Gao, J.; Ma, X.; Chen, O. Colloidal Synthesis and Charge Carrier Dynamics of $Cs_4Cd_{1-x}Cu_xSb_2Cl_{12}$ ($0 \leq x \leq 1$) Layered Double Perovskite Nanocrystals. *Matter* **2021**, *4* (9), 2936−2952.
(56) Cai, T.; Shi, W.; Hwang, S.; Kobbekaduwa, K.; Nagaoka, Y.; Yang, H.; Hills-Kimball, K.; Zhu, H.; Wang, J.; Wang, Z.; Liu, Y.; Su, D.; Gao, J.; Chen, O. Lead-Free $Cs_4CuSb_2Cl_{12}$ Layered Double Perovskite Nanocrystals. *J. Am. Chem. Soc.* **2020**, *142* (27), 11927−11936.
(57) Vargas, B.; Torres-Cadena, R.; Reyes-Castillo, D. T.; Rodríguez-Hernández, J.; Gembicky, M.; Menéndez-Proupin, E.; Solis-Ibarra, D. Chemical Diversity in Lead-Free, Layered Double Perovskites: A Combined Experimental and Computational Approach. *Chem. Mater.* **2020**, *32* (1), 424−429.
(58) Shannon, R. Revised Effective Ionic Radii and Systematic Studies of Interatomic Distances in Halides and Chalcogenides. *Acta Crystallogr.* **1976**, *32* (5), 751−767.
(59) Bai, T.; Yang, B.; Chen, J.; Zheng, D.; Tang, Z.; Wang, X.; Zhao, Y.; Lu, R.; Han, K. Efficient Luminescent Halide Quadruple-Perovskite Nanocrystals via Trap-Engineering for Highly Sensitive Photodetectors. *Adv. Mater.* **2021**, *33* (8), No. 2007215.
(60) Yang, B.; Han, K. Charge-Carrier Dynamics of Lead-Free Halide Perovskite Nanocrystals. *Acc. Chem. Res.* **2019**, *52* (11), 3188−3198.
(61) Arfin, H.; Kaur, J.; Sheikh, T.; Chakraborty, S.; Nag, A. Bi^{3+}-Er^{3+} and Bi^{3+}-Yb^{3+} Codoped $Cs_2AgInCl_6$ Double Perovskite Near-Infrared Emitters. *Angew. Chem., Int. Ed. Engl.* **2020**, *59* (28), 11307−11311.
(62) Pei, Y.; Tu, D.; Li, C.; Han, S.; Xie, Z.; Wen, F.; Wang, L.; Chen, X. Boosting Near-Infrared Luminescence of Lanthanide in $Cs_2AgBiCl_6$ Double Perovskites via Breakdown of the Local Site Symmetry. *Angew. Chem., Int. Ed. Engl.* **2022**, *61* (30), No. 202205276.
(63) Zhou, D.; Sun, R.; Xu, W.; Ding, N.; Li, D.; Chen, X.; Pan, G.; Bai, X.; Song, H. Impact of Host Composition, Codoping, or Tridoping on Quantum-Cutting Emission of Ytterbium in Halide Perovskite Quantum Dots and Solar Cell Applications. *Nano Lett.* **2019**, *19* (10), 6904−6913.
(64) Zhou, D.; Liu, D.; Pan, G.; Chen, X.; Li, D.; Xu, W.; Bai, X.; Song, H. Cerium and Ytterbium Codoped Halide Perovskite Quantum Dots: A Novel and Efficient Downconverter for Improving the Performance of Silicon Solar Cells. *Adv. Mater.* **2017**, *29* (42), No. 1704149.
(65) Vargas, B.; Torres-Cadena, R.; Rodríguez-Hernández, J.; Gembicky, M.; Xie, H.; Jiménez-Mier, J.; Liu, Y.-S.; Menéndez-Proupin, E.; Dunbar, K. R.; Lopez, N.; Olalde-Velasco, P.; Solis-Ibarra, D. Optical, Electronic, and Magnetic Engineering of ⟨111⟩ Layered Halide Perovskites. *Chem. Mater.* **2018**, *30* (15), 5315−5321.
(66) Yang, H.; Shi, W.; Cai, T.; Hills-Kimball, K.; Liu, Z.; Dube, L.; Chen, O. Synthesis of Lead-Free $Cs_4(Cd_{1-x}Mn_x)Bi_2Cl_{12}$ ($0 \leq x \leq 1$) Layered Double Perovskite Nanocrystals with Controlled Mn-Mn Coupling Interaction. *Nanoscale* **2020**, *12* (45), 23191−23199.
(67) Shi, S.; Sun, L. D.; Xue, Y. X.; Dong, H.; Wu, K.; Guo, S. C.; Wu, B. T.; Yan, C. H. Scalable Direct Writing of Lanthanide-Doped $KMnF_3$ Perovskite Nanowires into Aligned Arrays with Polarized Up-Conversion Emission. *Nano Lett.* **2018**, *18* (5), 2964−2969.
(68) Reisfeld, R.; Greenberg, E.; Jacoboni, C.; De Pape, R.; Jørgensen, C. K. Energy Transfer Between Managanese(II) and Erbium(III) in Various Fluoride Glasses. *J. Solid State Chem.* **1984**, *53* (2), 236−245.

https://doi.org/10.1021/jacs.3c11164
J. Am. Chem. Soc. 2024, 146, 3200−3209